Journal of Non-Newtonian Fluid Mechanics 296 (2021) 104628

Contents lists available at ScienceDirect

Journal of Non-Newtonian Fluid Mechanics

journal homepage: www.elsevier.com/locate/jnnfm

# Pore-scale simulation of viscous instability for non-Newtonian two-phase flow in porous media

Takshak Shende, Vahid Niasar, Masoud Babaei *

*Department of Chemical Engineering and Analytical Science, The University of Manchester, Manchester, United Kingdom*

## ARTICLE INFO

*Keywords:*
Non-Newtonian fluid
Meter model
Viscosity
Shear-thinning fluid
Weissenberg number
Heterogeneity
Porous media

## ABSTRACT

The impact of micro-heterogeneity on non-Newtonian two-phase flow is the focus of the present study. The direct numerical simulation of non-Newtonian fluids (modelled using shear stress-dependent Meter model) displacing oil in 3D Mt. Simon sandstone and 2D heterogeneous porous media were considered over a range of wettabilities (strong imbibition to strong drainage), capillary numbers and viscosity ratios. This study suggests that heterogeneity of the porous medium can potentially lead to an unstable fluid flow front (even after use of polymer). Therefore along with capillary number and viscosity ratio, heterogeneity is the governing factor for controlling viscous and capillary fingering, and it is crucial to account for the microscale heterogeneity of porous media to design polymer solution injection.

## 1. Introduction

Immiscible multiphase flow in porous media involving polymeric solutions has many applications specifically for enhanced oil recovery [1–3], and remediation of subsurface non-aqueous phase liquid (NAPL) contaminants [3,4]. Polymeric solutions, which have non-Newtonian rheology, is commonly utilised to displace NAPL or crude oil in the subsurface. The heterogeneity of the porous medium and shear-dependent rheology of non-Newtonian fluids make the multiphase flow more complex. The effectiveness of polymeric solutions to displace oil depend on physical and chemical parameters of oil, polymeric solutions and subsurface materials which vary spatially with time [5]. Although core-flood experiments on larger samples have been used to study polymeric macroscopic sweep efficiency [1], these experiments can hardly be used to gain pore-scale insights on the microscopic displacement of invading and displacing fluids.

Wettability, which is the fluid's ability to adhere to the solid surface in the presence of another fluid, is one of the key factors in two-phase flow dynamics in the porous medium. The contact angle ($\theta$) between the fluid–fluid interface and the solid surface determines which fluid (displaced or displacing) has a tendency to adhere to the solid surface. For example, in a porous medium wetted by water ($\theta < 90°$), the polymer fluid will adhere to the solid surface, while in a porous medium wetted by oil ($\theta > 90°$), the oil will adhere to the solid surface. Although fluid–fluid interactions during multiphase flow are influenced by the wettability of the solid surface [6], less attention is paid to the multiphase flow involving non-Newtonian fluids. Hatzignatiou et al. [7] conducted a polymer flood experiment on water and oil-wet Bentheim and Berea sandstone. They suggested that rock wettability strongly affects the polymer retention in the porous medium and influences the polymer front velocity. The authors postulated that the physical adsorption of polymer to the rock surface causes entrapment of polymer in the sandstone as they observed higher polymer retention in the water-wet Berea sandstone compared to the oil-wet Berea sandstone. Broseta et al. [8] reported reduction in the polymer adsorption in an oil-wet micromodel compared to a water-wet one. Jamaloei and Kharrat [9] reported that the displacement front's stability during polymer flooding depends on pore-morphology and wettability in a porous medium. Using magnetic resonance imaging technique, Romero-Zerón et al. [10] investigated the effects of wettability in water-wet and oil-wet rocks and reported higher oil recovery in strongly water-wet rocks using partially hydrolysed polyacrylamide solution. Ameli et al. [11] observed that salinity reduces the efficiency of oil recovery during polymer flooding, and the water-wet system gives favourable oil recovery compared to the oil-wet system. Eslami and Taghavi [12] demonstrated that the wettability affects the viscous fingering pattern formations and flow efficiency of the displacement using two-phase microfluidic experiments wherein Newtonian fluid was used to displace non-Newtonian fluid in a rectangular Hele-Shaw cell. Li et al. [13] visualised oil saturation in the oil-wet and water-wet rocks using magnetic resonance imaging and suggested that the polymer stripping mechanism dominates in an oil-wet rock.

* Corresponding author.
*E-mail address:* masoud.babaei@manchester.ac.uk (M. Babaei).

https://doi.org/10.1016/j.jnnfm.2021.104628
Received 28 May 2021; Received in revised form 26 July 2021; Accepted 2 August 2021
Available online 9 August 2021

Meybodi et al. [14] experimentally examined the effect of microscopic heterogeneity on West Paydar crude oil-recovery using polymeric partially hydrolysed polyacrylamide fluid. They found that water-wet and mixed wet porous medium could recover higher oil compared to oil-wet porous medium in most of the experiments; however, they also reported that the effects of micro-heterogeneity and porous medium's wettability on polymeric fluid-based oil recovery are case dependent [14]. Rodríguez de Castro et al. [15] studied the effect of xanthan gum concentration (0–2000 ppm) on silicon oil-displacement over a range of capillary numbers and mobility ratios in a heterogeneous hydrophilic 2D micromodel of porosity 60% and pore size distribution of 29 - 160 μm. The authors reported an increase in oil recovery with an increase in polymer concentration; however, they observed heterogeneity dependent viscous fingers in the 2D micromodel porous medium during polymer flooding over a range of xanthan gum concentration [15]. De et al. [16] experimentally investigated two-phase displacement of silicon oil using xanthan gum, hydrolysed polyacrylamide (HPAM) solution and viscoelastic surfactant fluid in a hydrophilic pillared (regularly arranged) micro-channel of porosity 75%. They reported the highest oil recovery using viscoelastic surfactant and HPAM compared to xanthan gum solution over a capillary number range. They suggested that the micro-sweep mechanism plays a vital role in non-Newtonian fluid-based oil displacement in the porous medium. Similarly, Nillson et al. [5] found that visco-elastic fluid and shear-thickening nanoparticle fluid displace more oil compared to the shear-thinning fluids. Parasa et al. [17], using confocal microscopy visualised HPAM polymer displacing oil in a 3D porous micromodel of porosity 45% and suggested that a non-Newtonian fluid's elastic turbulence leads to the additional oil recovery during polymer flooding. The recent studies of oil recovery with the aids of microfluidic experiments suggested micro-sweep of oil by polymeric solutions play a crucial role during polymeric flooding [16,18–20].

Although pore-scale wettability alteration simulation studies for the flow of Newtonian two-phase flow using Lattice Boltzmann [21] and Volume-of-fluids methods [22] are available in the literature, wettability effects on pore-scale non-Newtonian two-phase flow have not been carefully studied. Shi and Tang [23] carried out a two-phase flow simulation of a Newtonian fluid displacing a power-law fluid using the Lattice Boltzmann method in a porous medium composed of staggered square blocks. This study was carried out using power-law fluids, ignoring the Newtonian plateau at low shear values. Based on numerical simulation, Zhang and Yue [24] reported that visco-elasticity, the flow field, and the stress field determine the sweeping of an oil present in the dead-end by polymeric solutions. Zhong et al. [25] conducted two-phase simulations using the volume-of-fluid method in OpenFOAM to study the effects of elasticity on oil recovery. They concluded that elasticity of the non-Newtonian fluid enlarges sweep area and increases displacement efficiency. Using the same approach, Zhong et al. [26] investigated the effect of non-Newtonian fluid (based on the cross model) on the displacement of oil and reported that the polymeric solutions increase displacement efficiency by 8%–20%. Tsakiroglou [3] developed an inverse modelling numerical scheme to determine macroscopic flow parameters for two-phase flow where non-wetting shear-thinning fluid (modelled using Meter model) displaced Newtonian fluid in a porous medium and validated the same using unsteady two-phase experiments conducted on pore-network.

### 1.1. This study

Most of the studies reported above were carried out in simple homogeneous porous media; it is unlikely that such geometries will take into account micro-heterogeneity and true complexities as observed realistically. Pore-scale micro-heterogeneity significantly affects the microscopic displacement of fluid in the porous media. Only few studies [15–17,27,28] considered effects of micro-heterogeneity on polymeric fluid-induced oil displacement. The pore size in the real and heterogeneous porous medium can vary up to 2 orders of magnitude; thus, pore-scale velocity and viscosity in the porous media also vary significantly. This spatial variation of viscosity and velocity in the pore-spaces and capillarity govern the flow's stability. Thus, the main objective of this work is to determine how microscale heterogeneity and wettability of the porous medium govern the stability of polymeric fluid flow even for favourable viscosity ratios where the flow is stable. For this purpose, we utilise the volume-of-fluid based 'interFoam' solver of OpenFOAM for two-phase flow involving shear-stress dependent Meter model fluids. Meter model captures S-shaped rheology (*i.e.* power-law behaviour at intermediate shear values and Newtonian plateau at low and high shear values) of most of the shear thinning and shear thickening polymeric non-Newtonian fluids [29].

We validate the numerical approach adopted in the present work for the two-phase flow of the Meter model fluid using microfluidic experimental observation of air displacing non-Newtonian fluid in the Hele-Shaw cell. We study the effects of wettability alteration on the displacement behaviour of oil and a polymeric non-Newtonian fluid (polyacrylamide) over a range of porosities (with different heterogeneity levels), capillary numbers, polymer concentrations, and viscosity ratios in 2D and 3D porous media. The results substantiate that the complex interplay between pores geometry, rheology of the fluid, and capillary force regulate the stability of the two-phase fluid transport.

## 2. Numerical simulation

The Volume-of-Fluid (VoF) method, implemented in OpenFOAM [30] using interFoam solver, is used to simulate immiscible and incompressible two-phase fluid flow in a porous medium involving non-Newtonian fluids. The details of the VoF method implemented in OpenFOAM for two-phase flow displacement can be found at [26,31–35]. The shear viscosity ($\eta$) of the polymeric non-Newtonian fluid is defined using shear stress-dependent Meter model (Eq. (1)) [29,36,37],

$$\eta = \eta_\infty + \frac{\eta_0 - \eta_\infty}{1 + \left(\frac{\tau}{\tau_m}\right)^S} \tag{1}$$

where, $\eta_0$ [Pa s], $\eta_\infty$ [Pa s] and $\tau_m$ [Pa] are the zero-shear viscosity, the infinite shear viscosity, and the critical shear stress of the non-Newtonian fluid at which viscosity of the fluid drops to $\frac{\eta_0+\eta_\infty}{2}$, respectively. $S$ is the shear stress-dependent exponent of Meter model, which represent slope [29,37]. The characteristic time (*i.e.* longest relaxation time, $\lambda$) of the non-Newtonian fluid is $\lambda = \frac{\eta_0+\eta_\infty}{2\,\tau_m}$ [29,36]. For carrying out numerical simulation, Meter model is written as a function of shear rate as described in [37]. This is obtained by substituting $\tau = \eta_m \dot{\gamma}$ in Eq. (1), where $\eta_m = \frac{\eta_0+\eta_\infty}{2}$ is the viscosity of the fluid at $\tau_m$. The exponent of Meter model changes to $S^{-1}$:

$$\eta = \eta_\infty + \frac{\eta_0 - \eta_\infty}{1 + \left(\frac{\eta_0 + \eta_\infty}{2\,\tau_m}\,\dot{\gamma}\right)^{S^{-1}}} \tag{2}$$

### 2.1. Numerical scheme and the solver

We used PIMPLE (*i.e.* merged PISO-SIMPLE) algorithm for coupling of pressure and velocity [38]. Patankar et al. [39] proposed the Semi-Implicit Method for Pressure-linked equation (SIMPLE) algorithm to estimate steady-state solution, however, SIMPLE algorithm neglect velocity correction term. The Pressure-Implicit Splitting Operator (PISO) algorithm proposed by [40] consider velocity correction term. We refer to [38–41] for details on PIMPLE, SIMPLE, and PISO algorithms. The second-order implicit backward method was used to discretise the time scheme of the governing equations. The gradient term and divergence term were discretised using Gauss linear scheme. The Gauss linear uncorrected scheme was employed to discretise Laplacian term of governing equations. The pressure field and velocity field were solved

**Table 1**
The Meter model parameters of Separan AP30 fluid of [44] and polyisobutylene mixed in mineral oil (PIB) of [42] used for the numerical experiments.

| Parameter | Separan AP30 concentration | | PIB |
|---|---|---|---|
| | 0.50% | 0.05% | 500 ppm |
| $\eta_0$ [Pa s] | 4.350 | 0.260 | 0.055 |
| $\eta_\infty$ [Pa s] | 0.001 | 0.001 | 0.033 |
| $\tau_m$ [Pa] | 0.718 | 0.339 | 0.079 |
| $S$ | 1.471 | 1.190 | 3.8 |
| $\lambda$ [s] | 3.030 | 0.384 | 0.9 |

using GAMG solver and smoothSolver of the OpenFOAM. The convergence criterion of $10^{-7}$ was implemented for pressure and velocity fields. The average time-step was adjustable between $10^{-5}$ - $10^{-6}$ s to have a Courant number below 0.5. The Courant number is $C = \frac{u\,\Delta t}{\Delta x}$, here, $\Delta t$ is the time step and $\Delta x$ is length interval.

### 2.2. Initial and boundary conditions

Three sets of two-phase numerical simulations were conducted in the present work.

- Simulation of two-phase flow in square Hele-Shaw cell to validate the model against the experimental data of [42] for air displacing a non-Newtonian polymeric solution (500 ppm polyisobutylene mixed in mineral oil) in a partially saturated square Hele-Shaw cell at a constant pressure.
- Simulation of two-phase flow in three-dimensional Mt. Simon sandstone of [43] to study the effect of wettability on two-phase flow dynamics.
- Simulation of two-phase flow in homogeneous and heterogeneous polydisperse two-dimensional porous media.

SnappyHexMesh utility of OpenFOAM was used to generate meshes on porous media domain. No-slip boundary conditions were applied to the walls. For the first set of experiment, Hele-Shaw cell (square geometry of 150 mm length and gap spacing of 100 μm, porosity ($\phi$) = 1) was partially saturated with 500 ppm polyisobutylene (PIB) fluid at the centre with a volume of 100 $\mu$L (diameter of 0.025 m). Air was injected with a constant injection pressure at the centre and allowed to flow along the radial direction. The inlet has an inner diameter of 2.4 mm. We note that White and Ward [42] used a plastic shim to keep the desired spacing between two plates. We could not identify the geometry and exact location of the plastic shim in the experimental Hele-Shaw cell. Furthermore, an initial drop of PIB fluid placed at the centre of the Hele-Shaw fluid by [42] has slightly deviated from the centre; thus, PIB fluid was not uniformly distributed around the centre. Thus, the present simulation is not a replica of the experimental work of [42] as we could not implement the plastic shim spacer geometry and exact spatial saturation of PIB solution in the simulation setup. We modelled shear stress-dependent rheology of 500 ppm polyisobutylene mixed in mineral oil (PIB) using Meter model (see Fig. 1 and Table 1). We considered density of PIB as $\rho = 920$ kg/m$^3$. The interfacial tension (IFT) and contact angle between PIB and air were considered as 0.03 N/m and 60° due to absence of the same in the work of [42]. The density of viscosity and density of air were taken as $1.81 \times 10^{-5}$ Pa s and 1.225 kg/m$^3$, respectively.

For the second and the third sets of numerical experiments, the domain was fully saturated with silicon oil. Inlet injection velocity and constant pressure with zero gradients were applied to the porous medium domain's left and right boundary. Polyacrylamide solution (Seperan AP30 fluid, see Table 1 for Meter model parameter and Fig. 1) of Park et al. [37,44] was injected into the 3D domain of Mt Simon sandstone [37,43], and 2D domain of porous medium saturated with silicon oil (density: 970 kg/m$^3$, dynamic viscosity: 0.02 Pa s).

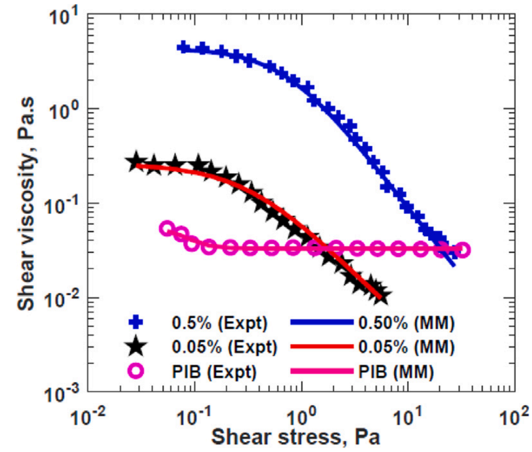


**Fig. 1.** Experimental shear viscosity–shear stress of 0.5% and 0.05% Separan AP30 fluid of [44] and PIB solution of [42] modelled using Meter model (MM) Eq. (1).

The details of 2D and 3D porous media domains used for simulations are given in Fig. 2 and Table 2. The interfacial tension between the polyacrylamide solution and silicon oil is 0.029 N/m [15]. We used ParaView 5.7.0 [45] to post-process the simulation data. Table 2 shows an average computation time for each simulation for the 2D and 3D domains along with the number of mesh points in the domain. We used 32 CPU cores in parallel and 16 CPU cores in parallel for the 3D and 2D simulations, respectively. Each CPU cores had a memory of 4GB. The simulations were computationally expensive as the number of grid points were larger than 3 million, and the time-step was between $10^{-5}$ to $10^{-6}$ s.

### 2.3. Capillary number, viscosity ratio and Weissenberg number

Capillary number is the ratio of viscous forces to the surface tension forces. Most of the literature uses the Darcy velocity of the injected fluid [22,33,46] instead of pore-scale velocity to estimate the Capillary number of a Newtonian fluid flow. The use of Darcy velocity to estimate Capillary number is widespread due to two reasons. Firstly, it is easy to measure experimentally compared to the pore velocity. Secondly, macroscopic properties of fluid flow in a porous medium are easy to analyse using Darcy's law for all practical purpose. However, since the interaction between capillary force and viscous forces during two-phase flow occurs at pore-scale. The capillary number must always be determined using pore-scale fluid flow properties (*i.e.*, velocity, viscosity, interfacial tension) to ensure that the capillary number represents the actual ratio between viscous forces and capillary forces.

In present work, the capillary number ($Ca_{\mathrm{N}}$) of a two-phase Newtonian fluid displacing Newtonian fluid flow is estimated using $Ca_{\mathrm{N}} = \frac{U_{\mathrm{i}}\,\eta_{\mathrm{i}}}{\sigma}$ [35,47]. The viscosity ratio ($M_{\mathrm{N}}$) for two-phase Newtonian fluids displacement is defined using $M_{\mathrm{N}} = \frac{\eta_{\mathrm{d}}}{\eta_{\mathrm{i}}}$ [35,47]. Here, $\eta_{\mathrm{i}}$ [Pa s] is the viscosity of the invading fluid, $\eta_{\mathrm{d}}$ [Pa s] is the viscosity of the displaced fluid, $U_{\mathrm{i}}$ [m/s] is the invading fluid's average velocity in the porous medium domain, $\sigma$ [N/m] is the interfacial tension between invading fluid and displaced fluid.

The shear viscosity of the non-Newtonian fluid in a porous medium varies spatially, thus, we define capillary number ($Ca_{\mathrm{NN}}$) of non-Newtonian fluid displacing Newtonian fluid as $Ca_{\mathrm{NN}} = \frac{U_{\mathrm{i}}\,\eta_{\mathrm{eff}}}{\sigma}$, and the viscosity ratio ($M_{\mathrm{NN}}$) using $M_{\mathrm{NN}} = \frac{\eta_{\mathrm{d}}}{\eta_{\mathrm{eff}}}$ [4,5,16,48,49]. Here, $\eta_{\mathrm{eff}}$ [Pa s] is the effective viscosity of the non-Newtonian fluid for a given set of flow conditions [29,37].

The Weissenberg number ($Wi$) is the ratio of the elastic forces to the viscous forces. $Wi$ for the flow of non-Newtonian fluid through confined space is defined as the product of the longest relaxation time ($\lambda$) of

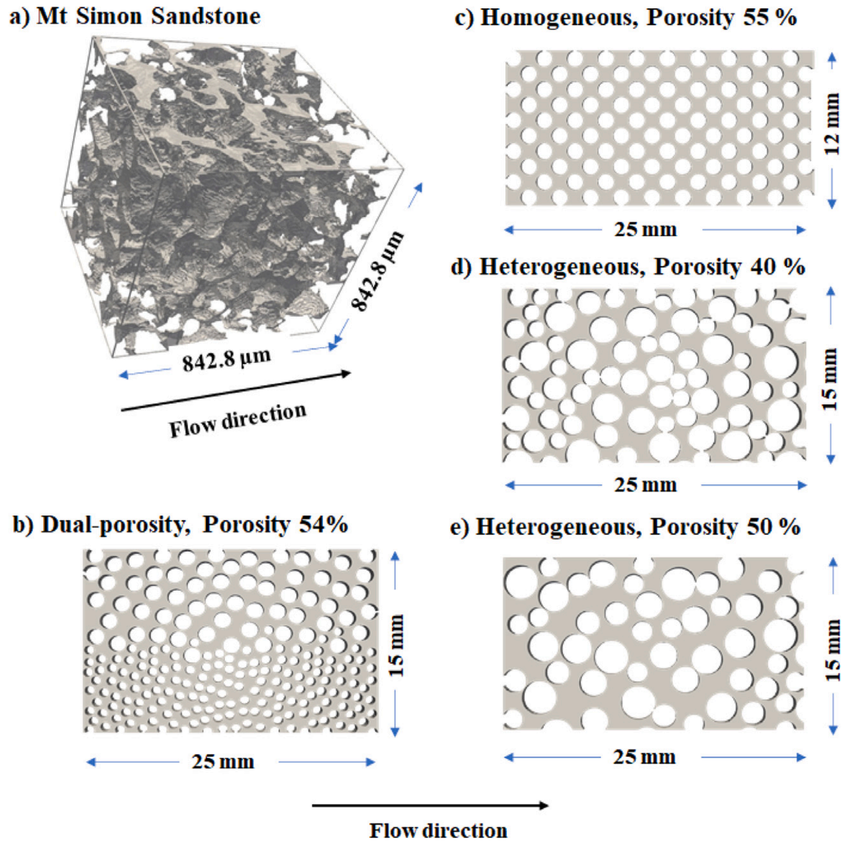


**Fig. 2.** Geometry of (a) segmented Mt Simon sandstone of size 842.8 μm ×842.8 μm ×842.8 μm, (b) heterogeneous 2D porous medium having duel-porosity, (c) homogeneous 2D porous medium having porosity 55%, (d) heterogeneous 2D porous medium having porosity 40%, and (e) heterogeneous 2D porous medium having porosity 50%. No-slip condition at solid surfaces and boundaries (except at inlet and outlet).

**Table 2**
Type of porous medium domains and computation time for the second and third numerical experiments.

| Type | Porosity ($\phi$) | Domain size | Pore size distribution | Mesh points | CPU time (h) |
|---|---|---|---|---|---|
| Mt Simon Sandstone (3D) | 0.24 | 842.8 μm × 842.8μm × 842.8 $\mu$m | 5–120 μm | 1,21,12,247 | 1,176 |
| Homogeneous (2D) | 0.55 | 25 mm × 12 mm | 350 μm | 43,19,174 | 168 |
| Heterogeneous (2D) | 0.54 | 25 mm × 15 mm | 30–710 μm | 3,,19,743 | 336 |
| Heterogeneous (2D) | 0.50 | 25 mm × 15 mm | 8.1–685 μm | 38,00,823 | 168 |
| Heterogeneous (2D) | 0.40 | 25 mm × 15 mm | 6.6–418 μm | 30,79,048 | 672 |

the polymeric solution and the shear rate (*i.e.* $Wi = \lambda\dot{\gamma}$) [5,50,51]. The shear rate of the fluid flow in a porous medium depends on the pore-morphology and fluid rheology, and varies significantly in the porous medium domain. Thus, we defined Weissenberg number ($Wi$) for the flow of polymeric solution in the porous medium as [5,50,52,53],

$$\mathrm{Wi} = \lambda\,\dot{\gamma}_{\mathrm{avg}} \tag{3}$$

here, $\dot{\gamma}_{\mathrm{avg}}$ is the volume-averaged shear rate over a porous medium domain saturated with non-Newtonian fluids. We estimated the volume-averaged velocity ($U_{\mathrm{avg}}$), volume-averaged effective viscosity ($\eta_{\mathrm{eff}}$), volume-averaged shear rate ($\dot{\gamma}_{\mathrm{avg}}$) of the fluid flow in a porous medium by integrating the pore-scale velocity value ($U$), viscosity value ($\eta$), shear rate value ($\dot{\gamma}$), respectively, over a pore-space filled with a non-Newtonian fluid ($V_P$) in the porous medium domain during two-phase flow. The representative upscaled value of the fluid properties for a given set of fluid flow condition in a porous medium depends on the pore-scale variation of the property. We have shown in the subsequent section that volume-averaged value can be used as a representative upscaled value of the pore-scale fluid-flow phenomenon.

## 3. Results and discussion

### 3.1. Convergence of numerical simulation

The grid convergence analyses were performed on different grid resolutions (50,000–500,000) using the same numerical scheme as given in Section 2.2. The grid convergence was performed on subsample (see Fig. 3) of porous medium having porosity of 54% at an injection rate of 0.01 m/s and time-step of $10^{-5}$ s. Fig. 3 shows comparison of average velocity and average viscosity of the polymeric fluid in a saturated domain as a percentage of the high resolution case for each grid size considered. Fig. 3 shows insignificant difference in the average velocity and viscosity after grid density 30 cells/μm$^2$. The Courant number was higher than 1 for grid size lower than 20 cells/μm$^2$. Although, computationally expensive, all simulations were carried out with a grid density higher than 50 cells/μm$^2$ to maintain convergence and accuracy. This resolution provided at-least 50 cells in the smallest pore-throat of the heterogeneous porous medium.

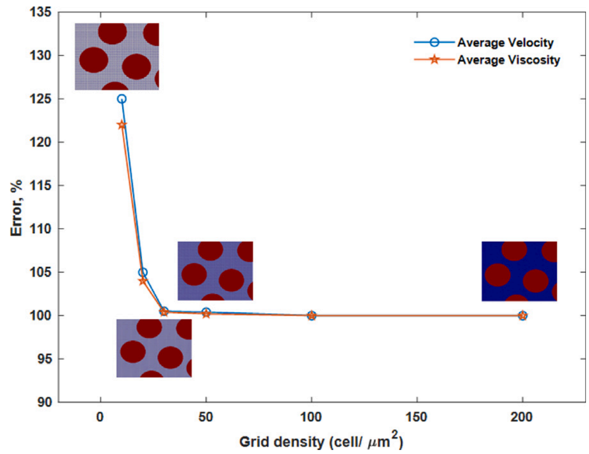


**Fig. 3.** Average velocities and average viscosity for each grid density. The error shows percentage of the average value attained compared to the highest grid resolution.

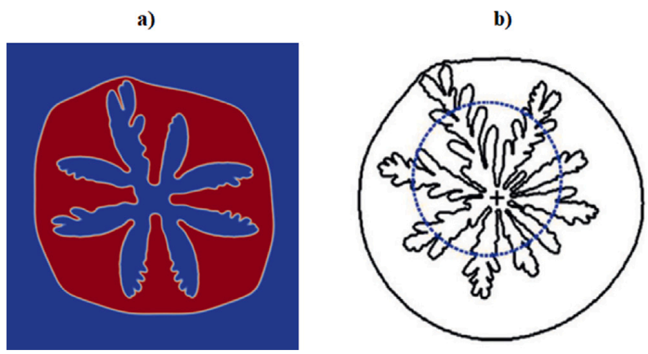


**Fig. 4.** Comparison of (a) the two-phase simulation of air displacing a non-Newtonian fluid (PIB polymeric fluid modelled using Meter model) in a partially filled radial Hele-Shaw cell, against (b) an experimental observation of White and Ward [42] at inlet pressure of 6900 Pa. Blue and red indicate air and PIB polymeric solution, respectively.

### 3.2. Validation of two-phase numerical modelling

Fig. 4 shows that the flow paths adopted by PIB–air interface in the numerical simulation and the Hele-Shaw experiment of [42] are not identical at the injection pressure of 6.9 kPa. This difference in the flow paths is expected due to the difference in the outlet boundary condition of [42] experiment and boundary condition adopted in the simulations described in Section 2.2. We note that the PIB fluid location in the Hele-Shaw cell was not uniformly distributed around the inlet during experiment and it was partially deviated from the centre as shown by the inner dotted line in Fig. 4(b). Moreover, fluid material parameters (*i.e.* interfacial tension, density and contact angle) used in the simulation may not be the same as in the experiments of [42].

Although the interface flow paths of numerical simulation and experiments are not identical, the fluid–fluid interface instability pattern is similar. The branches of the fingers formed during the simulation and the experiment follow the similar pattern. The fingers are formed either by tip splitting or side branching. The thinner fingers with side branches and smooth sides can also be observed in the simulations and the experiment. These results indicate that the Volume of Fluid method based two-phase simulation involving non-Newtonian fluid can be modelled using shear stress-dependent Meter model equation.

### 3.3. Pore-scale variation of velocity and viscosity

To quantify the variability of the flow of injected fluid within a heterogeneous porous medium (porosity 40%) at an injection rate of 0.01 m/s, we calculated probability density functions (PDF) of the velocity components along the longitudinal and transverse direction, velocity magnitude, and viscosity as shown in Fig. 5. Similar to the experimental observation of [46] for Newtonian fluid, Fig. 5c shows exponential decay of velocity magnitude of non-Newtonian fluid. Although flow along transverse is symmetric about $U_T = 0$, the distribution is non-Gaussian and decaying exponentially. Similarly, flow along longitudinal direction $U_L$ shows non-Gaussian distribution with exponential decay. The viscosity of the injected fluid also shows the non-Gaussian distribution. These results imply that flow in the heterogeneous porous medium is non-random and geometry of pore-space governs distribution of velocity and viscosity.

The probability density function of velocity magnitude could fit into the Beta distribution function. The mean and standard deviation of the velocity magnitude, estimated using Beta distribution function, were $3 \times 10^{-2}$ m/s and $4.1 \times 10^{-2}$ m/s. These results are consistent with a volume-average velocity ($2.97{\times}10^{-2}$ m/s) obtained after integrating the velocity magnitude value over a porous medium domain saturated with injected fluid. Similarly, PDF of viscosity value could fit into Gamma distribution function with a mean of 0.6 Pa s and standard deviation of 0.165 Pa s, and these values also agree with volume-averaged viscosity value of 0.61 Pa s. To take into pore-scale variability in the porous medium, we will report volume-averaged values and the standard deviation of velocity, viscosity, shear rate in the subsequent sections.

### 3.4. Mt. Simon sandstone

We simulated flow of 0.5% PAA polymeric solution displacing silicon oil through Mt Simon sandstone in the water-wet ($\theta = 30°$), intermediate-wet ($\theta = 90°$) and oil-wet ($\theta = 120°$) conditions. Table 3 shows average velocity, effective viscosity, the average shear rate of 0.5% PAA solution flow in the Mt Simon sandstone and corresponding $Ca$, $M$ and $Wi$ in water-wet, intermediate-wet and oil-wet domain. The $\eta_{\text{eff}}$ of polymeric solution at an injection rate of $10^{-3}$ m/s was on average 0.82 Pa s over a range of contact angles, thus, estimated $Ca$ on average was 4.19 $\times 10^{-2}$. Generally, for estimation of $Ca$ of polymeric fluid flow, the polymeric solution's zero-shear viscosity has been extensively used in the literature [1]. The estimated value of $Ca$ using zero-shear viscosity is 2.19 $\times 10^{-1}$ which is one order of magnitude greater than values gives in Table 3. We note that the $Ca$, $M$ and $Wi$ estimated in the present work could be considered as representative values for a given set of fluid flow conditions as these values are determined from direct numerical simulations data instead of unrealistic viscosity values (*i.e.* zero-shear viscosity) for given fluid flow conditions.

The PAA polymeric solution saturations (Fig. 6a,b,c) and simulation movie clip (Clip 1 of the Supporting Information) over a range of contact angle indicate that the flow path adopted by polymeric solution in water-wet, intermediate-wet and oil-wet porous medium are different. The oil saturation profiles (Fig. 6d,e,f) and PAA–oil interface profiles (Fig. 6g,h,i) in the Mt Simon sandstone indicate that an increase in the contact angles increases the distribution of small trapped oil fragments in the sandstone. The surface area of the PAA–oil interface at breakthrough was $5.57{\times}10^{-7}$ $m^2$, $7.76{\times}10^{-7}$ $m^2$, and $1.51{\times}10^{-6}$ $m^2$, at $\theta = 30°$, $\theta = 90°$, and $\theta = 120°$, respectively. Fig. 6j shows 25.71%, 32.44%, and 34.5% remaining oil saturation at breakthrough after injection of 0.5% PAA polymeric solution (injection rate at inlet of $10^{-3}$ m/s) in water-wet ($\theta = 30°$), intermediate-wet ($\theta = 90°$) and oil-wet ($\theta = 120°$) Mt Simon sandstone of [43], respectively.

Fig. 6k shows the pressure gradients during the simulation as a function of oil-saturation at a constant inlet injection rate of $10^{-3}$ m/s in the Mt Simon sandstone. These results imply that oil-wet condition requires higher pressure compared to water-wet condition to displace oil from heterogeneous Mt Simon sandstone. Furthermore, as the oil saturation decreases with time, the pressure required to maintain the constant

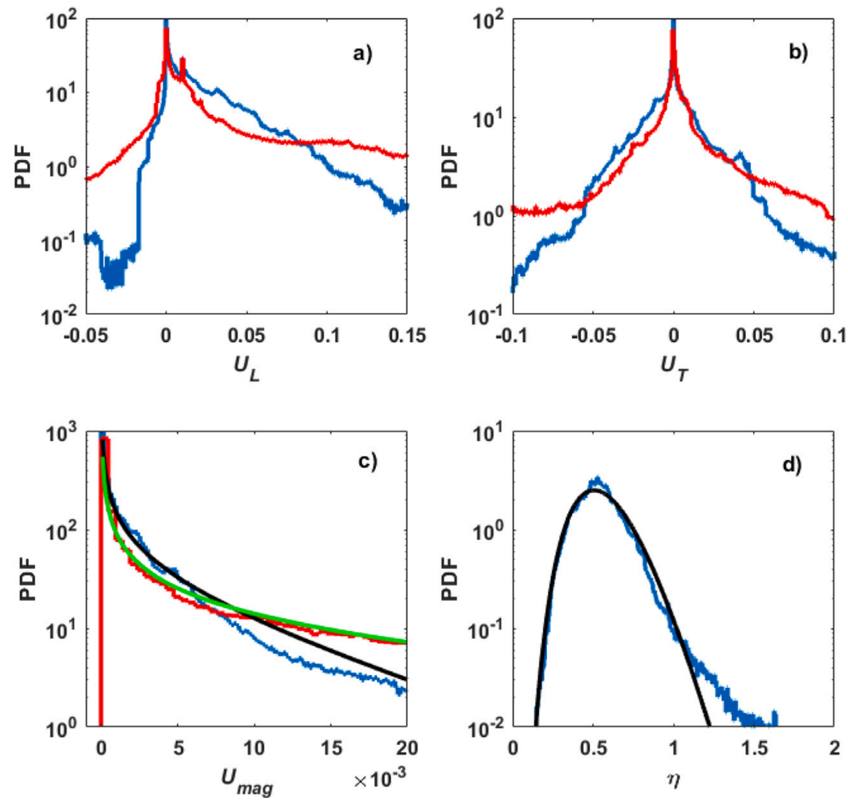


**Fig. 5.** Probability density function (PDF) of (a) velocity component in longitudinal direction ($U_L$, m/s), (b) velocity component in transverse direction ($U_T$, m/s), (c) velocity magnitude ($U_{mag}$, m/s), and (d) viscosity ($\eta$, Pa s) of injected fluid in the porous medium with porosity 40%. The data is over the domain saturated with injected fluid. Blue line indicates data of PAA fluid and red line indicate data of water. Black and green line in (c) indicate Beta distribution function fitting for PAA fluid and water, respectively. black line in (d) indicate Gamma function fitting with viscosity data. Injection rate is 0.01 m/s.

**Table 3**
Capillary number ($Ca$), viscosity ratio ($M$), Weissenberg number ($Wi$) of PAA-polymeric fluid flow in 3D Mt Simon sandstone.

| $\theta$ | $U_{avg}$ (m/s) | $\eta_{eff}$ (Pa s) | $\dot{\gamma}_{avg}$ (s$^{-1}$) | $Ca$ | $M$ | $Wi$ |
|---|---|---|---|---|---|---|
| 30° | $1.3 \times 10^{-3}$ | 0.8 | 161 | $3.59 \times 10^{-2}$ | $2.5 \times 10^{-2}$ | 487 |
| 90° | $1.5 \times 10^{-3}$ | 0.82 | 153 | $4.24 \times 10^{-2}$ | $2.44 \times 10^{-2}$ | 463 |
| 120° | $1.64 \times 10^{-3}$ | 0.83 | 104 | $4.75 \times 10^{-2}$ | $2.38 \times 10^{-2}$ | 315 |

flow rate increases. The simulation of PAA-solution displacing silicon oil suggests that the water-wet condition is favourable for oil recovery compared to the intermediate-wet or oil-wet conditions. We note that we did not observe stable fluid flow front in Mt Simon sandstone at the capillary number of $2.83 \times 10^{-2}$. Even though PAA polymeric solution with significantly high viscosity value, (*i.e.* with much lower viscosity ratio) was used to displace silicon oil, we observed fingers during fluid flow (Fig. 6a,b,c and simulation movie clip 1 in the SI). We note that fingers in Mt Simon sandstone are more visible in simulation movie clip 1 of the SI as compared to Fig. 6a,b,c. These fingers were mostly governed by the heterogeneity of the Mt. Simon sandstone.

### 3.5. Effect of heterogeneity

To explore whether heterogeneity of the porous medium affects the stability of polymeric fluid flow front and oil recovery, we simulated the two-phase flow of 0.5% PAA-polymeric solution displacing silicon oil and water displacing silicon oil in a homogeneous ($\phi$ : 0.55) and heterogeneous ($\phi$ : 0.40, 0.50, 0.54) porous media domain as shown in Fig. 7 at the constant injection rate of 0.01 m/s at inlet and contact angle of 30°. Although the injection rate of water and 0.5% PAA polymer was 0.01 m/s during simulation, the average velocity of the injected fluid in the porous medium was higher and varied depending on the porous medium's heterogeneity (see Table 4). Average velocity in the porous medium increased with decrease in the porosity. The capillary number of PAA fluid injection is two orders of magnitude greater than water injection.

Fig. 7a to d depict that water injection at an injection rate of 0.01 m/s shows fingers in the porous medium and fluid front follows preferential flow paths. Width of the fingers in the homogeneous porous medium is much larger than those in the heterogeneous porous medium. Moreover, the width of the fingers becomes thinner with the decrease in the porosity.

The homogeneous or orderly porous medium (circular staggered), as in Fig. 7e, shows stable polymeric fluid flow front at the injection rate of 0.01 m/s. On the contrary, the disorderly or heterogeneous porous medium shows instability in the fluid flow front (Fig. 7f and g) at the same injection rate. The oil-saturation profiles (Fig. 7f and g) of heterogeneous porous medium show that the fragments of residual oil are present in the porous medium.

Fig. 7d and h show fluid flow front of water and PAA fluid in heterogeneous porous medium with two porosities. The upper portion of porous medium had porosity of 57% (PSD: 75 μm–710 μm) and bottom portion had porosity of 50% (PSD: 30 μm–520 μm) with overall porosity of 54%. Fig. 7d shows that length of finger in upper portion is much larger than in bottom portion of the medium. Water prefers

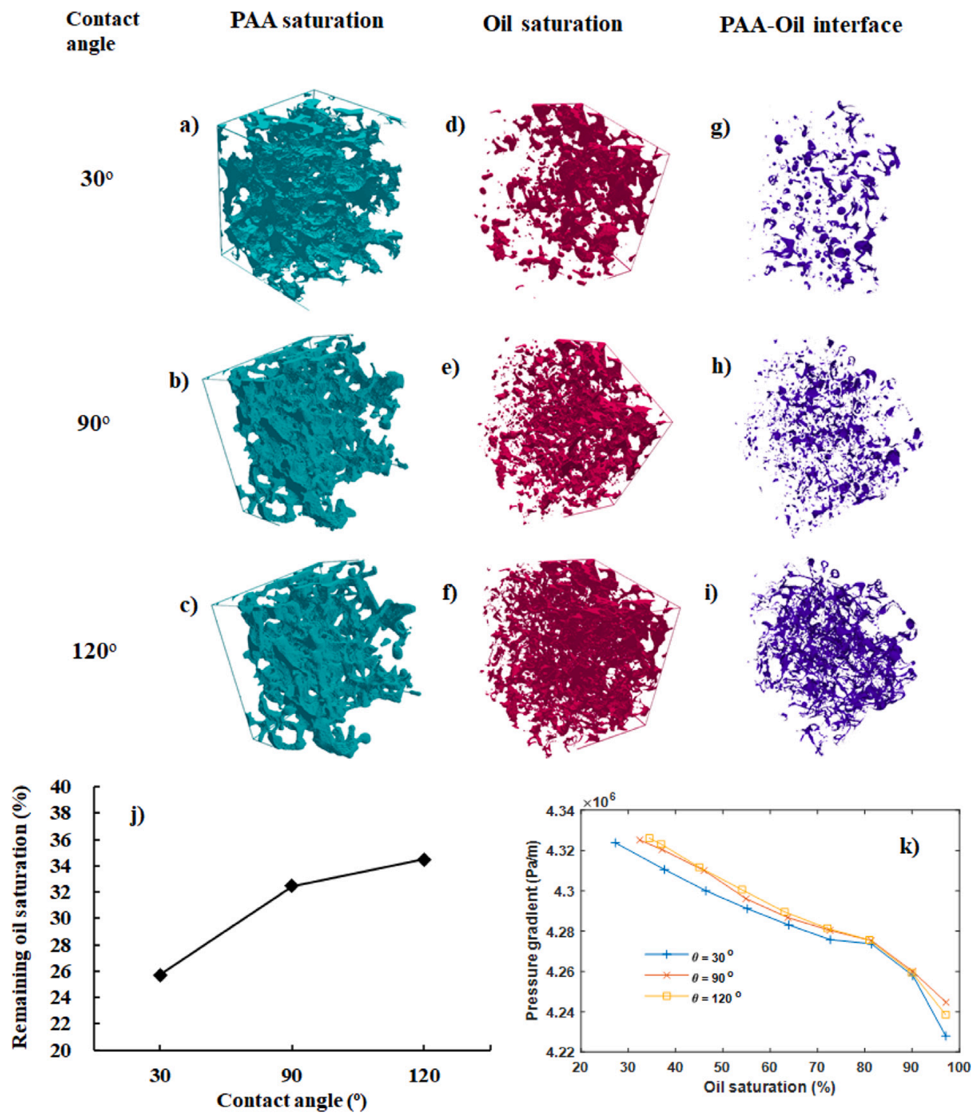


**Fig. 6.** Effect of contact angle on the remaining oil saturation in Mt Simon sandstone. Figure (a, b, c) show the distribution of polyacrylamide (PAA) fluid saturation at different contact angles, (d, e, f) silicone oil saturation profiles, and (g, h, i) profile of PAA–oil interface profiles. (j) Remaining oil saturation at breakthrough. (k) Pressure gradient as a function of oil saturation (pressure gradient is the pressure difference between inlet and outlet of Mt Simon sandstone). Injection rate is $10^{-3}$ m/s.

**Table 4**
Capillary number ($Ca$), viscosity ratio ($M$) of 2D homogeneous and heterogeneous porous medium.

| Porous medium | Injection fluid | $U_{avg}$ (m/s) | $\eta_{\mathrm{eff}}$ (Pa s) | $Ca$ | $M$ |
|---|---|---|---|---|---|
| $\phi$ : 0.40 | Water | 0.048 ± 0.101 | 0.001 | $1.65 \times 10^{-3}$ | 20 |
| | 0.5% PAA | 0.030 ± 0.041 | 0.61 ± 0.17 | $6.22 \times 10^{-1}$ | $3.3 \times 10^{-2}$ |
| $\phi$ : 0.50 | Water | 0.031 ± 0.054 | 0.001 | $1.07 \times 10^{-3}$ | 20 |
| | 0.5% PAA | 0.019 ± 0.022 | 0.76 ± 0.17 | $4.87 \times 10^{-1}$ | $2.63 \times 10^{-2}$ |
| $\phi$ : 0.55 | Water | 0.017 ± 0.022 | 0.001 | $5.80 \times 10^{-4}$ | 20 |
| | 0.5% PAA | 0.014 ± 0.008 | 0.53 ± 0.066 | $2.47 \times 10^{-1}$ | $3.78 \times 10^{-2}$ |
| $\phi$ : 0.54 | Water | 0.033 ± 0.030 | 0.001 | $1.15 \times 10^{-3}$ | 20 |
| | 0.5% PAA | 0.019 ± 0.016 | 0.64 ± 0.23 | $4.12 \times 10^{-1}$ | $3.12 \times 10^{-2}$ |

to flow through areas having higher porosity as compared to the low porosity area. On the contrary, polymeric fluid shows stable fluid flow front in both areas of porous medium. The fluid flow front of high porosity area could reach breakthrough early as compared to fluid flow front in low porosity area. These results indicate that porosity variation of the porous medium influences the fluid flow front and preferential path. The remaining oil saturation at breakthrough in two-porosity porous medium is comparable with the remaining oil saturation in the porous medium with porosity 50% at same injection rate. The spatial location of smaller and larger throats in the porous medium governs the porous medium's fingering. Fig. 7f,g have small throats in between the larger throats, on the contrary, such small throats in between the larger throats are not available in Fig. 7h. These results imply that fingering in Fig. 7f and g (visible more in movie clip 2) is due to the presence of smaller throats in between the larger throats. The pressure required to displace fluid through smaller throats is much higher than the larger throats/pores. The injected fluid prefers to move through larger throats first and creates imbalance at the fluid–fluid interface. This leads to an instability at fluid–fluid interface and fingers appear as polymeric injected fluid advances towards the outlet.

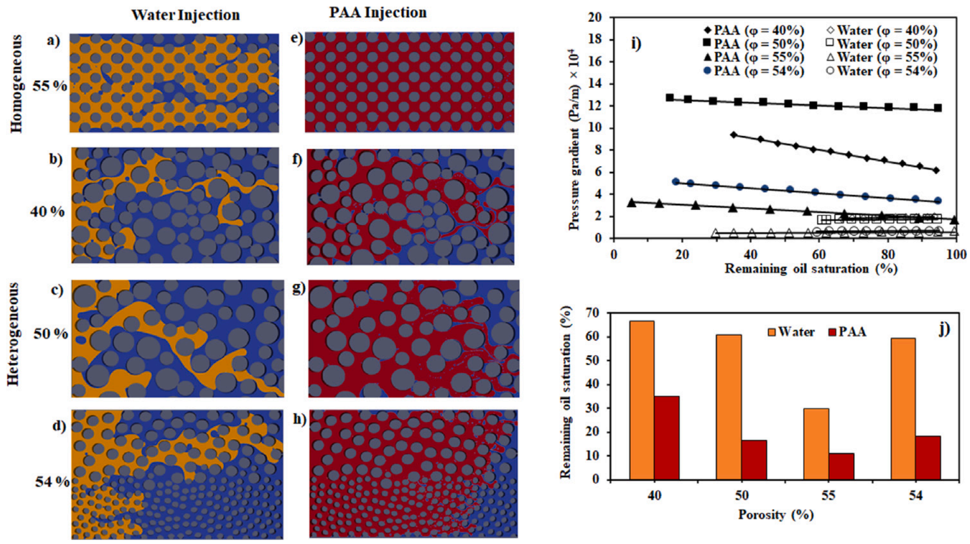


**Fig. 7.** Effect of heterogeneity on oil recovery during water injection and 0.5% polyacrylamide injection in the 2D porous medium. Figure (a,b,c,d) show distribution of water (in yellow) and silicon oil (in blue) saturation, and (e,f,g,h) distribution of polyacrylamide (PAA) (red) and silicon oil (in blue) saturation at breakthrough over a range of porosity (40%, 50%, 55%, 54%) and heterogeneity. (i) Pressure gradient as a function of oil saturation (pressure gradient is the pressure difference between inlet and outlet). (j) Remaining oil saturation (%) as a function of porosity at the breakthrough. $\theta$ is 30°, constant injection rate at inlet is $10^{-2}$ m/s.

In water-wet porous medium and at the high injection rate, we observed that the silicon oil detaches itself from the porous medium surface, moves into the pore-space centre, and surrounds itself with a polymeric solution (see simulation movie clip 2 in the supporting information). These small and larger fragments of silicon oil then move along with polymeric solution towards the outlet. The path of these small oil fragments depends on the pore size and morphology of the porous medium. Oil fragments prefer to move through pores having large sizes. We note that the mechanism mentioned above helps to recover residual oil using polymeric solutions even after the early breakthrough of a polymeric solution and viscous fingering at high injection rate.

### *3.6. Effect of contact angle and PAA concentration*

The effect of viscosity ratio at a constant injection velocity of $10^{-2}$ m/s on oil displacement was investigated by injecting polymeric fluid, having PAA concentration of 0, 0.05%, 0.5% in water, in a silicon oil-saturated 2D porous medium of porosity 40% as shown in Fig. 8a. Similarly, effect of viscosity ratio at a constant injection velocity of $10^{-3}$ m/s on oil displacement was evaluated over a range of contact angles in a dual-porosity medium as shown in Fig. 8b. The numerical experiment was carried out by keeping static contact angle of fluid interface with the solid surface as 30°, 90°, 120° which represent porous media flow from strong imbibition to strong drainage. The viscosity ratio for a displacement experiment with water, PAA-0.05%, PAA-0.5% were 20, 0.22, 0.032, respectively over a range of contact angles. Similarly, the capillary number for a displacement were $2.13{\times}10^{-3}$, $1.16{\times}10^{-1}$, $6{\times}10^{-1}$ for water, PAA-0.05%, PAA-0.5%, respectively. The Weissenberg number of the fluid flow was higher than 150. Although the injection rate at the inlet was constant (*i.e.* $10^{-2}$ m/s), the viscosity ratio decreased, and the capillary number increased with an increase in the PAA-concentration. These results indicate that balance of capillary forces and viscous forces in porous medium varies with variation in the rheology of the non-Newtonian fluids.

Fig. 8a depicts that an increasing concentration of the polymeric solution increases the oil recovery for the $\phi$ = 40% porous medium. The fluid flow front of water shows finger at the capillary number of $2.13 \times 10^{-3}$, on the contrary, more stable fluid front (but still with some fingers) can be observed after addition of PAA-polymeric solution in water. Addition of PAA in water decreased the viscosity ratio and increased the capillary number by 2 to 3 orders of magnitude. Fig. 8 shows that an increase in the static contact angle decreases the oil recovery over a range of PAA-concentrations. At oil-wet condition ($\theta >$ 120°), many regions with trapped oil in the polymeric solution were observed in the porous medium. On the contrary, a minimal amount of oil was trapped in the polymeric solution under the water-wet and intermediate-wet conditions (< 90°). The average velocity of water in the 2D porous medium was six times (i.e. $6.12{\times}10^{-2}$ m/s) of the inlet injection velocity ($10^{-2}$ m/s), whereas the average velocity of the polymeric solution ranged from $3.07{\times}10^{-2}$ to $3.9{\times}10^{-3}$ m/s over a range of contact angle and PAA concentration. Fig. 8b shows that addition of PAA in water increased the oil recovery over a range of contact angles in the dual-porosity medium at capillary number of $7.5{\times}10^{-2}$ and injection rate of $10^{-3}$ m/s. Fig. 8b shows stable fluid flow front with PAA fluid over a range of contact angles, on the contrary, water shows fingers in upper portion of the porous medium over a range of contact angles. Water could not flow through the bottom portion of the porous medium. We note that flow paths adopted by water and polymeric solution in the porous medium vary with the contact angle.

The difference between the behaviours of PAA solutions for 40% and dual-porosity media shows the importance of taking into account the heterogeneity at pore scale even for the stable polymeric solutions. Previous work on the continuum scale proposed that the macro-sweep is the primary oil recovery mechanism using the polymeric solution and micro-sweep plays an insignificant role [1].

## 4. Conclusion

We used Volume-of-Fluid based method to simulate the two-phase flow of non-Newtonian fluid in porous media. To describe the polymeric solution's rheology, we implemented a shear-stress dependent Meter model in the 'interfoam' solver of OpenFOAM. The Meter model-based simulation of Newtonian fluid displacing non-Newtonian fluid in a partially saturated Hele-Shaw cell was compared with a Hele-Shaw experiment of White and Ward [42] for validation. The pattern of the instability of the fluid–fluid interface (*i.e.* tip-splitting and side branching fingers) observed in the simulation, and the experiments of the White and Ward [42] were similar.

We simulated the displacement of oil by polymeric solution over a range of wettability conditions, heterogeneity, capillary number and

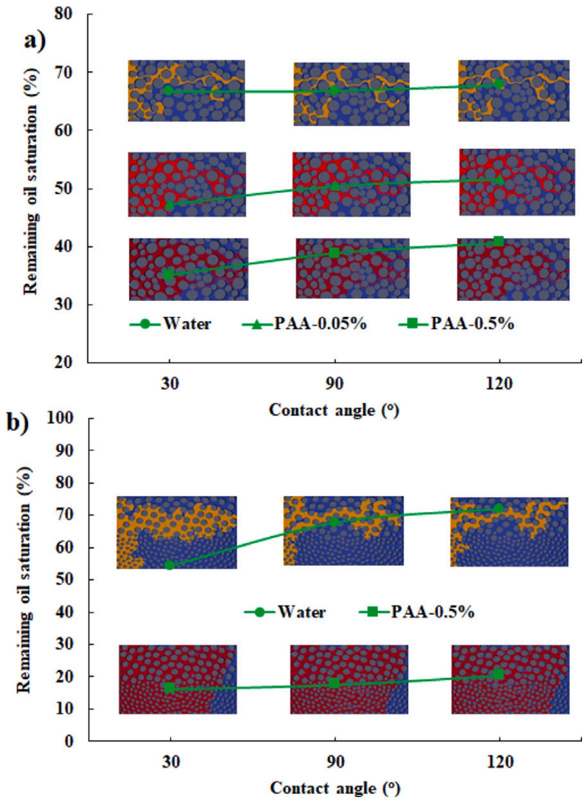


**Fig. 8.** Effect of contact angle and PAA concentration on oil recovery during water injection and polyacrylamide injection in a 2D porous medium, (a) porosity 40% at an inlet injection rate of $10^{-2}$ m/s, (b) dual porosity, 54% at inlet injection rate of $10^{-3}$ m/s. Figure shows distribution of water (in yellow) and silicon oil (in blue) and polyacrylamide (PAA) (red) at breakthrough.

viscosity ratio. The present work results suggest that heterogeneity of the porous medium governed the fingering during polymeric fluid-oil two phase fluid flow. Increasing the capillary number and viscosity ratio increases the oil recovery over a range of wetting conditions (*i.e.*, strong imbibition to strong drainage). Heterogeneity of the porous medium leads to the unstable fluid flow front (even after use of polymer). This suggests that along with capillary number and viscosity ratio, heterogeneity is the governing factor for controlling viscous and capillary fingering.

Visco-elasticity plays a vital role in the displacement of a polymeric solution. The Weissenberg number ($Wi$) of more than 140 in the porous medium implies that the micro-sweep of the oil by polymeric solution depends on the visco-elasticity of the polymeric solution. These results agree with reported experimental observations [16]. In future, we will study the effect of wettability of the porous medium and visco-elasticity of the polymeric solution on micro-sweep of oil using microfluidic experiments and two-phase simulation using linear Phan–Thien—Tanner model.

## Declaration of competing interest

The authors declare that they have no known competing financial interests or personal relationships that could have appeared to influence the work reported in this paper.

## Acknowledgement

The authors would like to acknowledge the assistance given by Research IT and the use of the Computational Shared Facility at the University of Manchester. T.S. would like to acknowledge Rajashri Shahu Maharaj Foreign Scholarship, United Kingdom from Government of Maharashtra, India for Ph.D. studies at the University of Manchester.

## Appendix A. Supplementary data

Supplementary material related to this article can be found online at https://doi.org/10.1016/j.jnnfm.2021.104628.

## References

[1] K.S. Sorbie, Polymer-Improved Oil Recovery, Springer Science & Business Media, 2013.
[2] C.D. Tsakiroglou, A methodology for the derivation of non-Darcian models for the flow of generalized Newtonian fluids in porous media, J. Non-Newton. Fluid Mech. 105 (2–3) (2002) 79–110.
[3] C.D. Tsakiroglou, Correlation of the two-phase flow coefficients of porous media with the rheology of shear-thinning fluids, J. Non-Newton. Fluid Mech. 117 (1) (2004) 1–23.
[4] L. Zhong, M. Oostrom, T.W. Wietsma, M.A. Covert, Enhanced remedial amendment delivery through fluid viscosity modifications: Experiments and numerical simulations, J. Contam. Hydrol. 101 (1–4) (2008) 29–41.
[5] M.A. Nilsson, R. Kulkarni, L. Gerberich, R. Hammond, R. Singh, E. Baumhoff, J.P. Rothstein, Effect of fluid rheology on enhanced oil recovery in a microfluidic sandstone device, J. Non-Newton. Fluid Mech. 202 (2013) 112–119.
[6] B. Zhao, C.W. MacMinn, R. Juanes, Wettability control on multiphase flow in patterned microfluidics, Proc. Natl. Acad. Sci. 113 (37) (2016) 10251–10256.
[7] D.G. Hatzignatiou, H. Moradi, A. Stavland, Polymer flow through water-and oil-wet porous media, J. Hydrodyn. 27 (5) (2015) 748–762.
[8] D. Broseta, F. Medjahed, J. Lecourtier, M. Robin, Polymer adsorption/retention in porous media: Effects of core wettability and residual oil, SPE Adv. Technol. Ser. 3 (01) (1995) 103–112.
[9] B.Y. Jamaloei, R. Kharrat, Fundamental study of pore morphology effect in low tension polymer flooding or polymer–assisted dilute surfactant flooding, Transp. Porous Media 76 (2) (2009) 199–218.
[10] L. Romero-Zeron, S. Ongsurakul, L. Li, B. Balcom, Visualization of the effect of porous media wettability on polymer flooding performance through unconsolidated porous media using magnetic resonance imaging, Pet. Sci. Technol. 28 (1) (2010) 52–67.
[11] F. Ameli, M.R. Moghbeli, A. Alashkar, On the effect of salinity and nano-particles on polymer flooding in a heterogeneous porous media: Experimental and modeling approaches, J. Pet. Sci. Eng. 174 (2019) 1152–1168.
[12] A. Eslami, S. Taghavi, Viscous fingering of yield stress fluids: The effects of wettability, J. Non-Newton. Fluid Mech. 264 (2019) 25–47.
[13] M. Li, L. Romero-Zeron, F. Marica, B.J. Balcom, Polymer flooding enhanced oil recovery evaluated with magnetic resonance imaging and relaxation time measurements, Energy Fuels 31 (5) (2017) 4904–4914.
[14] H.E. Meybodi, R. Kharrat, M.N. Araghi, Experimental studying of pore morphology and wettability effects on microscopic and macroscopic displacement efficiency of polymer flooding, J. Pet. Sci. Eng. 78 (2) (2011) 347–363.
[15] A.R. de Castro, M. Oostrom, N. Shokri, Effects of shear-thinning fluids on residual oil formation in microfluidic pore networks, J. Colloid Interface Sci. 472 (2016) 34–43.
[16] S. De, P. Krishnan, J. Van Der Schaaf, J. Kuipers, E. Peters, J. Padding, Viscoelastic effects on residual oil distribution in flows through pillared microchannels, J. Colloid Interface Sci. 510 (2018) 262–271.
[17] S. Parsa, E. Santanach-Carreras, L. Xiao, D.A. Weitz, Origin of anomalous polymer-induced fluid displacement in porous media, Phys. Rev. Fluids 5 (2) (2020) 022001.
[18] A.M. Howe, A. Clarke, D. Giernalczyk, Flow of concentrated viscoelastic polymer solutions in porous media: effect of MW and concentration on elastic turbulence onset in various geometries, Soft Matter 11 (32) (2015) 6419–6431.
[19] A. Clarke, A.M. Howe, J. Mitchell, J. Staniland, L. Hawkes, K. Leeper, Mechanism of anomalously increased oil displacement with aqueous viscoelastic polymer solutions, Soft Matter 11 (18) (2015) 3536–3541.
[20] J. Mitchell, K. Lyons, A.M. Howe, A. Clarke, Viscoelastic polymer flows and elastic turbulence in three-dimensional porous structures, Soft Matter 12 (2) (2016) 460–468.
[21] T. Akai, M.J. Blunt, B. Bijeljic, Pore-scale numerical simulation of low salinity water flooding using the lattice Boltzmann method, J. Colloid Interface Sci. 566 (2020) 444–453.
[22] R. Aziz, V. Joekar-Niasar, P.J. Martínez-Ferrer, O.E. Godinez-Brizuela, C. Theodoropoulos, H. Mahani, Novel insights into pore-scale dynamics of wettability alteration during low salinity waterflooding, Sci. Rep. 9 (1) (2019) 1–13.
[23] Y. Shi, G. Tang, Non-Newtonian rheology property for two-phase flow on fingering phenomenon in porous media using the lattice Boltzmann method, J. Non-Newton. Fluid Mech. 229 (2016) 86–95.

[24] L.-j. Zhang, X.-a. Yue, Displacement of polymer solution on residual oil trapped in dead ends, J. Cent. South Univ. Technol. 15 (1) (2008) 84–87.

[25] H. Zhong, Y. Li, W. Zhang, H. Yin, J. Lu, D. Guo, Microflow mechanism of oil displacement by viscoelastic hydrophobically associating water-soluble polymers in enhanced oil recovery, Polymers 10 (6) (2018) 628.

[26] H. Zhong, Y. Li, W. Zhang, D. Li, Study on microscopic flow mechanism of polymer flooding, Arab. J. Geosci. 12 (2) (2019) 56.

[27] E. Vermolen, M. Van Haasterecht, S. Masalmeh, A systematic study of the polymer visco-elastic effect on residual oil saturation by core flooding, in: SPE EOR Conference At Oil and Gas West Asia, Society of Petroleum Engineers, 2014.

[28] C. Xie, W. Lv, M. Wang, Shear-thinning or shear-thickening fluid for better EOR?—A direct pore-scale study, J. Pet. Sci. Eng. 161 (2018) 683–691.

[29] T. Shende, V.J. Niasar, M. Babaei, Effective viscosity and Reynolds number of non-Newtonian fluids using Meter model, Rheol. Acta 60 (2021) 11–21.

[30] H. Jasak, OpenFOAM: open source CFD in research and industry, Int. J. Naval Archit. Ocean Eng. 1 (2) (2009) 89–94.

[31] R. Aziz, V. Niasar, H. Erfani, P.J. Martínez-Ferrer, Impact of pore morphology on two-phase flow dynamics under wettability alteration, Fuel 268 (2020) 117315.

[32] D. Niblett, A. Mularczyk, V. Niasar, J. Eller, S. Holmes, Two-phase flow dynamics in a gas diffusion layer-gas channel-microporous layer system, J. Power Sources 471 (2020) 228427.

[33] A.Q. Raeini, B. Bijeljic, M.J. Blunt, Numerical modelling of sub-pore scale events in two-phase flow through porous media, Transp. Porous Media 101 (2) (2014) 191–213.

[34] M. Tembely, W.S. Alameri, A.M. AlSumaiti, M.S. Jouini, Pore-scale modeling of the effect of wettability on two-phase flow properties for Newtonian and non-Newtonian fluids, Polymers 12 (12) (2020) 2832.

[35] H.S. Rabbani, V. Joekar-Niasar, T. Pak, N. Shokri, New insights on the complex dynamics of two-phase flow in porous media under intermediate-wet conditions, Sci. Rep. 7 (1) (2017) 1–7.

[36] D.M. Meter, R.B. Bird, Tube flow of non-Newtonian polymer solutions: Part I. Laminar flow and rheological models, AIChE J. 10 (6) (1964) 878–881.

[37] T. Shende, V. Niasar, M. Babaei, Upscaling non-Newtonian rheological fluid properties from pore-scale to Darcy's scale, Chem. Eng. Sci. 239 (2021) 116638.

[38] F. Moukalled, L. Mangani, M. Darwish, The Finite Volume Method in Computational Fluid Dynamics, Vol. 6, Springer, 2016.

[39] S.V. Patankar, D.B. Spalding, A calculation procedure for heat, mass and momentum transfer in three-dimensional parabolic flows, in: Numerical Prediction of Flow, Heat Transfer, Turbulence and Combustion, Elsevier, 1983, pp. 54–73.

[40] R.I. Issa, Solution of the implicitly discretised fluid flow equations by operator-splitting, J. Comput. Phys. 62 (1) (1986) 40–65.

[41] J.H. Ferziger, M. Perić, R.L. Street, Computational Methods for Fluid Dynamics, Vol. 3, Springer, 2002.

[42] A.R. White, T. Ward, Constant pressure gas-driven displacement of a shear-thinning liquid in a partially filled radial Hele–Shaw cell: Thin films, bursting and instability, J. Non-Newton. Fluid Mech. 206 (2014) 18–28.

[43] A.H. Kohanpur, M. Rahromostaqim, A.J. Valocchi, M. Sahimi, Two-phase flow of $CO_2$-brine in a heterogeneous sandstone: Characterization of the rock and comparison of the lattice-Boltzmann, pore-network, and direct numerical simulation methods, Adv. Water Resour. 135 (2020) 103469.

[44] H. Park, M. Hawley, R. Blanks, The flow of non-Newtonian solutions through packed beds, Polym. Eng. Sci. 15 (11) (1975) 761–773.

[45] J. Ahrens, B. Geveci, C. Law, Paraview: an end-user tool for large data visualization, in: The Visualization Handbook, Vol. 717, (8) Elsevier Oxford, UK, 2005.

[46] S.S. Datta, H. Chiang, T. Ramakrishnan, D.A. Weitz, Spatial fluctuations of fluid velocities in flow through a three-dimensional porous medium, Phys. Rev. Lett. 111 (6) (2013) 064501.

[47] R. Lenormand, E. Touboul, C. Zarcone, Numerical models and experiments on immiscible displacements in porous media, J. Fluid Mech. 189 (1988) 165–187.

[48] S. Shahsavari, G.H. McKinley, Mobility and pore-scale fluid dynamics of rate-dependent yield-stress fluids flowing through fibrous porous media, J. Non-Newton. Fluid Mech. 235 (2016) 76–82.

[49] N.B. Lu, C.A. Browne, D.B. Amchin, J.K. Nunes, S.S. Datta, Controlling capillary fingering using pore size gradients in disordered media, Phys. Rev. Fluids 4 (8) (2019) 084303.

[50] C.A. Browne, A. Shih, S.S. Datta, Pore-scale flow characterization of polymer solutions in microfluidic porous media, Small 16 (9) (2020) 1903944.

[51] R. Poole, The Deborah and Weissenberg numbers, Rheol. Bull. 53 (2) (2012) 32–39.

[52] C.A. Browne, A. Shih, S.S. Datta, Bistability in the unstable flow of polymer solutions through pore constriction arrays, J. Fluid Mech. 890 (2020).

[53] D. Kawale, G. Bouwman, S. Sachdev, P.L. Zitha, M.T. Kreutzer, W.R. Rossen, P.E. Boukany, Polymer conformation during flow in porous media, Soft Matter 13 (46) (2017) 8745–8755.